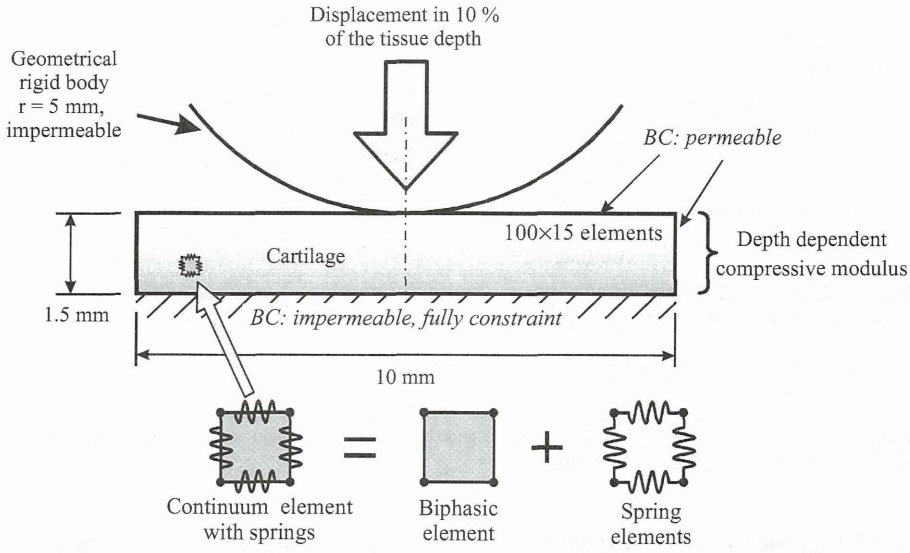

Fig. 4. The dimension of the model was 1.5 mm thickness and 10 mm length as a typical shape of the experimental specimen. The metallic cylindrical indenter was of 5 mm radius by geometrical rigid body. Horizontal and vertical fibrils were represented by a spring element SPRINGA.

contact region. The friction coefficient μ_{eq} [21] between the geometrical rigid indenter and the solid phase was set to zero. The compressive displacement was applied at the center of indenter with 10% of depth of the tissue model at the speed of the same 5%, 2%, 1% per second as that in experiment. It is important factor which constitutive properties are incorporated into representative material model for the calculation. In this study, we modeled the following constitutive compositions for the model. Firstly, the management of the surface seepage for exuding water content was implemented by user subroutine of ABAQUS using FLOW function (user subroutine to define nonuniform seepage coefficient and associated sink pore pressure for consolidation analysis). In the area covered by the cylindrical indenter the seepage coefficient of surface was set to zero to prevent flowing, whereas in the other area the seepage coefficient was set to one as a sufficient large value [46]. It was reported that the inhomogeneous cartilage property through depth direction promoted the effect of the interstitial fluid support [47]. Depth-dependent apparent Young's modulus of solid phase was introduced into our model, in which each layer in the FE model had each depth-specific modulus calculated by Eq. (2). It was expected that the effect of the surface amorphous layer [39] was partly incorporated in the depth-dependent Young's modulus in terms of a mechanical property, since Young's modulus of the top surface layer was lowest through depth direction in our observation shown later. Hydraulic permeability is well dependent as a function of strain [17]. For instance, Li incorporated the strain dependence of the permeability k into their FE model [24] by

$$k = k_0 \exp\left(M \frac{e-e_0}{1+e_0}\right) \tag{3}$$

where e_0 is an initial void ratio, e is the current void ratio, k_0 is the initial permeability at $e=e_0$, and M is a constant representing an effectiveness on the compaction. The initial void ratio e_0 as a constant value was set to 4, which represents that the proportion of the water content is 80%. Strain of solid phase is written by is $\varepsilon=(e-e_0)/(1+\varepsilon_0)$. Collagen fibril network, which was assumed to resist only tensile strain in this study, generates the sharp peak stress immediately after compression [24]. In recent computational analysis using spherical indenter, it was reported that deep vertical collagen fibril plays an important role on the reactional stiffness of the tissue especially in the transient period of a physiological condition [36]. In our model, as shown in Fig. 4, horizontal and vertical fibrils were represented by spring element SPRINGA (axial spring between two nodes, whose line of action is the line joining the two nodes) of the software, in which the spring elements were configured to generate reaction force only in the tensile direction. In this study, the stiffness K of the spring elements was simplified to the uniform value over the tissue and both in horizontal and vertical direction.

In summation, the variables for the curve fitting on FEM calculation were total apparent Young's modulus E_0, initial permeability k_0, compaction effect on permeability M, and collagen stiffness K. In other words, we tried to reduce the representation of the time-dependent reaction force of the cartilaginous tissue into these 4 variables within our compressive configuration, which aimed at a physiological condition in terms of compressive speed and amount. Depth-dependent local strain $E(x)$ was separately acquired as a typical value by the platen compression test written in Section 2.2. The curve fitting was executed by repetition of trial calculations and by visual confirmation with superposing the calculations on the experimental results. The threshold for automatic time integration in the estimation of material properties was specified of 10 kPa for UTOL, which regulates time integration period not to exceed the change of pore pressure by UTOL value within one increment. The NLGEOM parameter was turned on to take account of geometrical nonlinearity. Note again that the experimental results for estimating material properties were acquired from definite displacement compression by a positional control of the cylindrical indenter.

2.5. Finite element analysis for sliding cylindrical indenter

The constitutive material properties estimated and modeled in Section 2.4 were consequently applied to the analysis of sliding cylindrical indenter over cartilage surface. The dimension of the tissue model used in this section was 1.5 mm thickness and 25 mm length, shown in Fig. 5. The metallic cylindrical indenter that was slid over cartilage surface was of 5 mm radius. The biphasic tissue was modeled by CPE4RP and the mesh size was chosen as 0.1 mm square. Hence the total number of the elements was 3750 (250×15). The bottom of the model was fixed and impermeable. The other surface was not fixed and basically permeable except for contact region, in which the seepage coefficient within contact

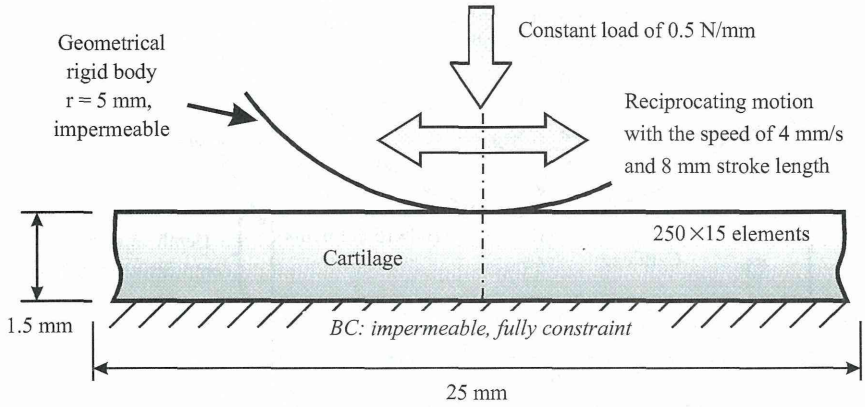

Fig. 5. The load of 0.5 N/mm was applied at the center of the cylindrical indenter and then the load was held constant. The reciprocating motion was introduced for the loaded indenter with the speed of 4 mm/s over a stroke length of 8 mm.

region was set to zero as written previously. One of the differences of compressive condition from Section 2.4 was that the indentation was performed by force, not position. The load of 0.5 N/mm was applied at the center of the cylindrical indenter with a ramp time of 1 s and then the load was held constant for further 92 s. Initial horizontal position of the indenter was at the center of the tissue surface. In the condition of sliding cylindrical indenter, the reciprocating motion was introduced for the loaded indenter with the speed of 4 mm/s over the stroke length of 8 mm during 92 s, which results in 23 cycles of reciprocation. In order to evaluate the sliding effect on the interstitial fluid pressurization, the static loading of the same 0.5 N/mm over entire period of simulation was also examined without any sliding motion in the simple creep-deformation simulation by the cylindrical indenter. The threshold for automatic time integration during the sliding period was specified of 1000 kPa for UTOL due to the limitation of calculation time, however maximum length of time integration was limited to 0.05 s. The other parameters were equal to the model in Section 2.4.

3. Results

3.1. Measurement of local strain

It is known that equilibrium local strain of cartilage tissue in compressive test varies from articular surface to deep zone, in which the surface zone is largely deformed in equilibrium condition [13,15,16]. In this study, a single image set on the relation between before compression and at equilibrium condition was examined to obtain local strain distribution through depth direction. Fig. 6(a) shows the local compressive strain plotted in normalized depth position, in which the position 0 means the surface. The average strain of the solid phase ε_0 was 9.90% in this experiment. Using Eq. (1), the local strain $\varepsilon(x)$ was acquired as the function of relative position x by

$$\varepsilon(x) = 0.462e^{-6.53x} + 0.0284 \quad (4)$$

It was observed that the tissue near the top surface was largely compressed by more than 40% strain. In this study, only $\varepsilon(x)$ and ε_0 were utilized in following FEM study to determine the variation of Young's modulus $E(x)$ through depth direction using Eq. (2).

3.2. Estimation of material property using FEM

In considering that the cylindrical indenter was used for the estimation of material properties, it would be appropriate that the

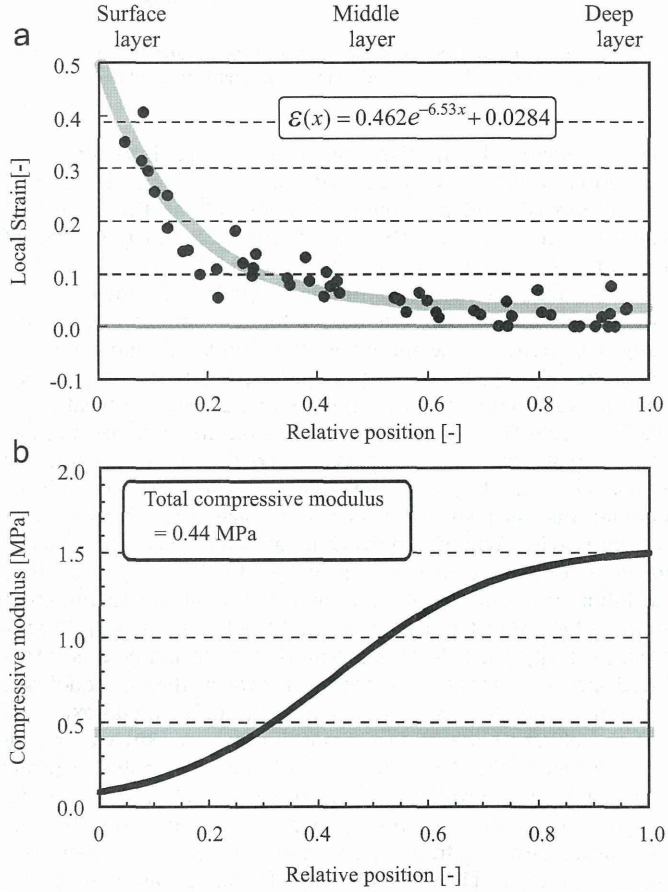

Fig. 6. (a) The local strain distribution through depth direction. The average strain of the solid phase was estimated by 9.90% in this experiment. (b) Compressive modulus distribution, when the bulk modulus is 0.44 MPa.

reaction force (not stress) was suitable for evaluating the curve fitting. Fig. 7 shows the experimental results of the cylindrical indentation (N=9), variance of experimental data and the results of curve fitting by the FEM calculation. The depth of the cartilaginous tissue of subchondral specimens, the width and the length were 1.53 ± 0.14, 2.48 ± 0.19, and 8.46 ± 1.95 mm (average $\pm$ variance), respectively. Note that the resultant curve fittings in different compressive speed shown in Fig. 7(a)–(c) were derived from the single parameter set of the material properties estimated in this study. The curve fitting was generally performed by following procedure, which may include an insightful affair on

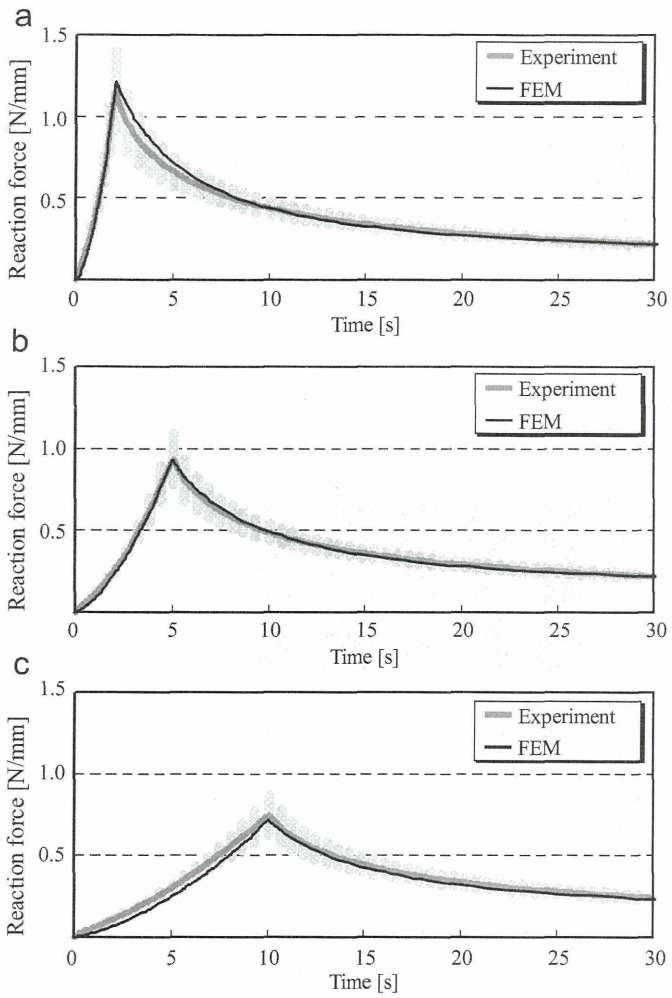

Fig. 7. The experimental results of the cylindrical indentation (N=9), variance of experimental data and the results of curve fitting of FEM calculation. Total compressive displacement of the indenter was 10% of the tissue depth at the cylindrical apex of the indenter. (a) 2 s, (b) 5 s and (c) 10 s compression.

how each parameter representing constitutive material property works functionally over the time-dependent reaction force.

As the time approaches to equilibrium period, the total compressive Young's modulus predominantly governs the total reaction force, because interstitial fluid pressure subsides. The total apparent Young's modulus of the solid phase E_0 was approximately estimated by the experimental reaction force at 180 s (not shown in this report). Then, the combination of $\varepsilon(x)$ and ε_0 with E_0 provides the distribution of apparent Young's modulus $E(x)$ for the curve fitting, by Eq. (2). Since the peak reaction force at the end of the compressive motion is clearly sensitive to the spring stiffness K, the spring stiffness was roughly identified here. Consequently, the rapid decrease of the reaction force immediately after compression for about 4 s well represents a relatively larger value of the initial permeability k_0. Without the compaction effect from the parameter M in Eq. (3), stress relaxation seemed to be faster than that of the experimental result. The modulation of the parameter M leads to the adjustment of stress relaxation in latter period. The repetition of these procedures would recurrently result in an acceptable curve fitting between the experimental result and the FEM calculation. Although small corrections of the parameters were required for the good fitting over different compressive speed, the curve fitting for 5 s compression shown in Fig. 7(b) basically found a reasonable value over the other compressive speed. While the objective data for the curve fitting on estimating the representative material properties was an average of time-dependent reaction force from 9 specimens, the data by a single specimen also showed fine fitting to FEM calculation over the different compressive speeds. The resultant parameters are shown in Table 1. Although the permeability of initial condition k_0 of 29.43×10^{-15} m^4/N s might be relatively larger value than a typical value of the permeability in other FEM research, large value for the initial permeability have been reported in some past research, in which the permeability was estimated by fitting FEM calculation to experimental result [17]. From our result with the parameter M of 38, the value $K=2.0\times10^{-15}$ m^4/N s is obtained in the compressive strain of 7% by Eq. (3). If the total apparent Young's modulus of the solid phase E_0 has the resultant value of 0.44 MPa, the distribution of apparent Young's modulus along the depth direction is plotted as shown in Fig. 6(b).

3.3. FEM analysis on the effect of migrating contact area and the constitutive parameters

Fig. 8 shows the result of FEM simulation on the effect of migrating contact area and the constitutive parameters. Index character A–E represents which the constitutive components were included in the FE model, shown in Fig. 8(b); e.g. the character E indicates that the distribution of compressive Young's modulus, the compaction effect on permeability and the reinforcement of spring elements were included in the model. If the distribution of apparent Young's modulus along depth direction was not included in the model, the apparent Young's modulus of 0.44 MPa as a bulk property was homogeneously applied to all the elements. If the compaction effect on permeability was not included, permeability in the model always remained in the initial value k_0. The vertical axis of the bar graphs in Fig. 8 represents the supporting force N/mm by the tissue. Total load support in each condition was summed up to 0.5 N/mm, because normal load of the indenter was held constant by 0.5 N/mm after the first compressive loading. Percentage numbers attached just above the bar graphs show the proportion of fluid load support to the total load.

Fig. 8(a) shows the proportion of load support immediately after compression of 1 s ramp loading. The distribution of apparent Young's modulus of the solid phase promoted the ratio of the fluid support. The reinforcement by spring elements was also effective to enlarge the ratio of the fluid support in comparing the conditions D with B. Fig. 8(c) shows the load support at 92 s after the end of ramp loading in the case that the indenter did not move from initial horizontal position. The compaction effect on permeability sustained the fluid support in comparing the conditions C and E with the others. In the condition without the compaction effect, permeability was constant in the initial permeability k_0. The value k_0 was thought to be a peculiar one in which the tissue was fully swelled on the surface of the bulk

Table 1
Material and kinematic properties estimated and used in the model of a cylindrical indenter sliding over cartilage.

Parameter	Value
Young's modulus (E_0)	0.44 MPa
Poisson's ratio	0.125
Initial permeability (k)	29.43×10^{-15} m^4/N s
Compaction effect on permeability (M)	38
Void ratio	4.0 (80% interstitial fluid)
Spring stiffness (K)	3.5 MPa
Sliding velocity	4 mm/s
Sliding stroke	$\pm$4 mm about the center
Seepage coefficient	1 mm^3/N s—flow 0 mm^3/N s—no flow,
Normal load on indenter	0.5 N/mm

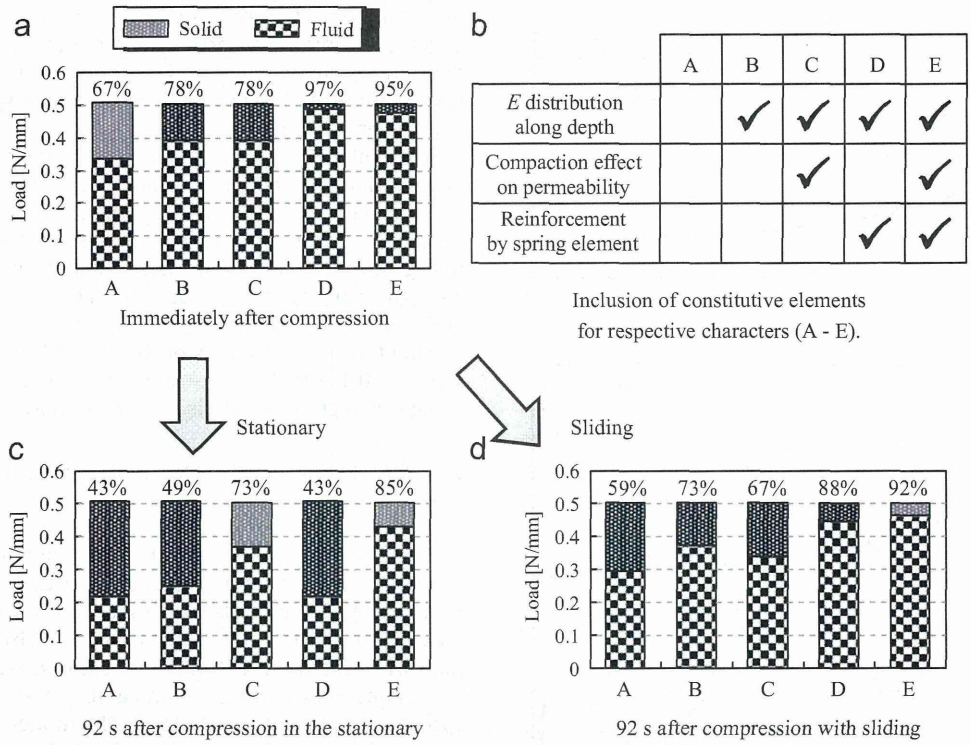

Fig. 8. (a) The result of FEM simulation on the effect of migrating contact area and the constitutive parameters. (b) Index characters A–E represents the constitutive components included in the FE model. The bar graph (a) shows the proportion of load support at immediately after compression. The graphs (c) and (d) show that of stationary indenter and moving indenter at 92 s, respectively.

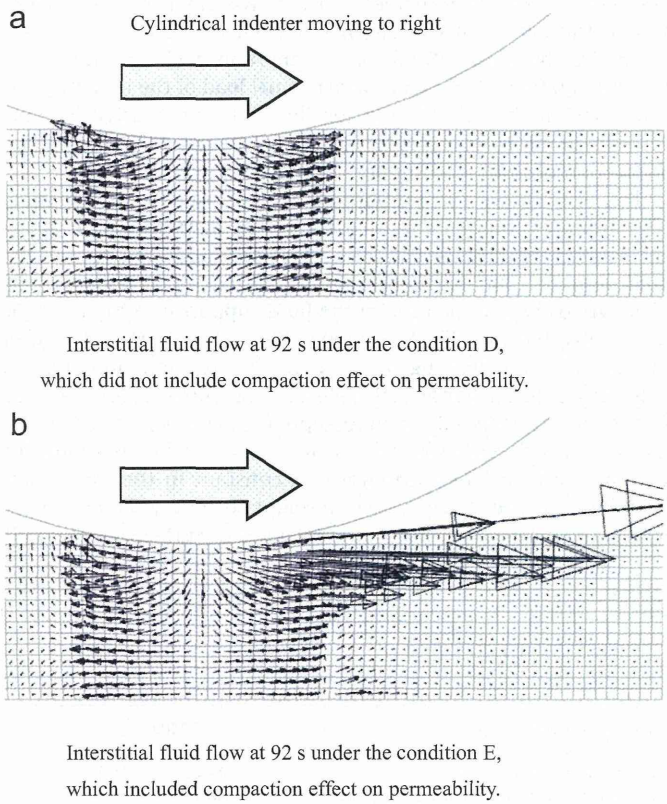

Fig. 9. Interstitial fluid flow at 92 s where the indenter was moving right. The compaction effect on permeability seemed to change the fluid flow.

tissue. Relative lower ratio of the fluid support in the condition D may be caused by this peculiar value k_0. Fig. 8(d) shows the load support with the sliding motion of the cylindrical indenter.

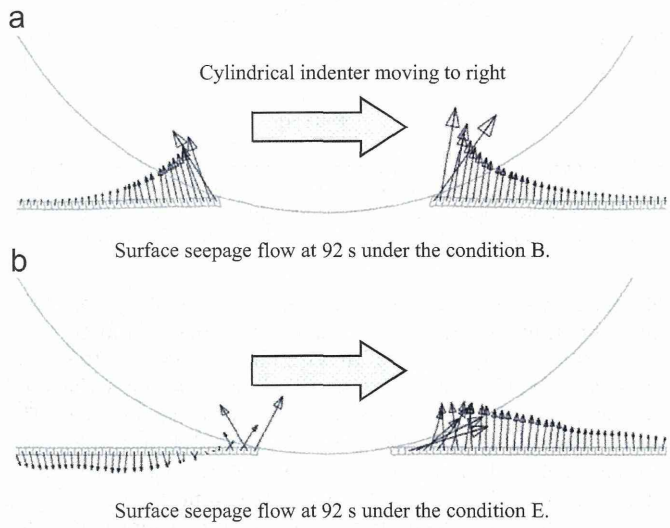

Fig. 10. The surface seepage of the flow. In this figure, the scale of the arrow representing fluid flow is 20 times larger than that in Fig. 9. The model including the spring reinforcement, which represents the collagen network, showed the drawing of the fluid behind the indenter. In this figure, the elements just under the contact area were removed to easy visibility for the surface seepage.

The time period of 92 s means that the indenter locates at the horizontal center of the tissue surface after 23 cycles of reciprocating motion. In sliding condition, the rubbing surface experienced a re-swelling period, since the contact area migrated over the tissue surface. As a whole, the fluid support was increased in comparing Fig. 8(c) except for the condition C. While the condition D drastically improved the ratio of the fluid load support, the condition C slightly decreased the fluid load support.

In observing interstitial fluid flow, the model including the compaction effect on permeability showed a particular flow

distribution, in which the interstitial fluid near the surface flowed forward in the moving direction of the cylindrical indenter. A typical result is shown in Fig. 9. The scale of the arrow representing fluid flow is the same in Fig. 9(a) and (b). This particular flow was probably due to the quick decrease of the permeability from the compaction effect written by Eq. (3), because the forward region was not so compressed than the region just under the apex of the cylindrical indenter. In observing the seepage flow on the tissue surface, the model including the reinforcement by spring elements showed an interesting result. The model including the spring reinforcement exuded the interstitial fluid in the forward surface of the indenter, whereas the fluid flow in the backward region was drawn in the tissue near the indenter shown in Fig. 10. This phenomenon was obscure in the model without the reinforcement by spring elements, which hopefully represents the tensile strengthening of the cartilaginous tissue by the collagen network.

4. Discussion

In the measurement of local strain at equilibrium state, large compressive strain was observed near the tissue surface. Apparent compressive Young's modulus was estimated under unconfined compression of semi-cylindrical specimen. The research concerning the inhomogeneity of the compressive modulus had been studied by several researchers. The method for estimating local strain by the correlation of microscopic images was utilized to estimate depth-dependent local strain without cutting the tissue into the stack of thin slices through depth direction. Using image correlation method, variation of the equilibrium local strain of full-thickness articular cartilage with subchondral bone was estimated in the past by a confined compression setup by Schinagl. In terms of aggregate modulus, the compressive modulus of first 125 μm layer from intact surface and the 250 μm thick layer adjacent to the subchondral bone were reported by 0.21 times and 5.6 times of the total bulk compressive modulus, respectively [13]. The local strain data from full-thickness tissue was consequently incorporated in a FE model to analyze stress relaxation behavior on the effect of depth-dependent compressive modulus [28]. Although an unconfined compression of semi-cylindrical osteochondral specimen was conducted in this study, the apparent compressive Young's modulus at surface and at bottom of the full-thickness articular cartilage were estimated to be 0.20 and 3.4 times of the total bulk property with a small extrapolation shown in Fig. 6(b). In a similar unconfined compression of semi-cylindrical geometry being removed subchondral bone, the compressive Young's modulus in the deep layer was reported to be about 2 MPa and had up to 10 times larger value than that in the surface layer [15]. In this study, a single data from one correlative image set was managed to find the local strain distribution for mainly re-confirming previous reports. Although absolute value was not completely congruent with the result of the other reports, the relative value of the compressive modulus in the surface layer to the bulk modulus was not so different from that shown in other report. Actually, the total apparent Young's modulus E_0, which regulated the absolute value of $E(x)$ shown in Eq. (2), was estimated from our experimental data by curve fitting using FEM simulation shown in Fig. 7, whereas the local strain distribution $\varepsilon(x)$ was utilized to transform the value E_0 into Young's modulus distribution $E(x)$. Since the purpose of this study is to examine how the constitutive material properties express the function of the cartilaginous tissue as a load-bearing material, authors thought that the local strain distribution acquired in this study would be acceptable in terms of the analysis concerning the integration of each constitutive mechanical property.

The identification of material properties utilizing the curve fitting was achieved with visually good conformation to the experimental data by the insightful procedure written in Section 3.2. From our experiences, we never succeeded in fitting FEM result to the time-dependent reaction force of the experimental indentation test without the effect of the compaction on permeability. In this study, four constitutive parameters, total apparent Young's modulus E_0, initial permeability k_0, compaction effect of permeability M and collagen stiffness K, were included for reproducing the mechanical behavior of articular cartilage in terms of the time-dependent reaction force. In this experiment, the influence of surface seepage was included by the geometrical condition of the cylindrical indenter. Although we could not insist that these parameters represented almost all mechanical behavior of the cartilaginous tissue, it was notable that the representation of the tissue in this study well conformed to the three different time-dependent reaction force in relatively physiological compressive speed. There would be generally 3 types of reason on dispersing experimental data. Firstly, there was a dispersion derived from an individual difference of each tissue. In looking into a single trial, the peak stress at the end of the ramp compression seemed to be very sensitive to compressive speed and displacement. Initial short load of 0.05 N just before the compression was applied to make sure a stable contact. Moreover, each specimen was exposed to three different compressive speeds following swelling interruption, where repeatability of the experiment was consistently required. Precise control of compressive speed and displacement was appropriately performed in the electro-mechanical tester with feedback control developed in our laboratory. While we experienced fine fitting of the reaction force between the experimental result and the FEM simulation, experimental data by single specimen basically showed the same level of fine fitting to FEM calculation over the different compressive speeds.

The initial permeability k_0 was estimated to be a relatively larger value than that in another report that utilized curve fitting of FEM simulation [24]. On the other hand, Jurvelin reported the permeability of a large value in small compressive strain and a drastic change of the permeability as the function of strain [17]. One of the reasons why the large initial permeability was estimated in this study might belong to the geometry of the cylindrical indentation, in which the surface seepage of the interstitial fluid was allowed just around the indenter. In other words, the surface for the exudation was simply large near the indenter or near the path of fluid flow. A degree of swelling was also the factor of variance on the initial permeability, which might include an osmotic phenomenon. In this study, the specimen was soaked in PBS for 30 min after compression test to recover shape and swelling level of the tissue in considering small size of the specimen. The inclusion of compaction effect on permeability successfully improved the conformity of the curve fitting. We applied 10% strain at the apex of the cylindrical indenter in experimental compression test. Although the compaction effect in larger strain field was not assured in this study, the effect above 10% strain was extrapolated by Eq. (3).

In all FE model employed in the curve fitting and consequent sliding simulation, Poisson's ratio of 0.125 for the solid phase was accepted as a typical value. It was thought that Poisson's ratio of the cartilaginous tissue varies through depth direction with anisotropic property. Since subchondral bone was preserved in our experimental specimens, lateral deformation of the bottom layer was constrained by the presence of subchondral bone. Cartilage-on-bone structure affects its micro-anatomical response on internal strain distribution [48]. The constraint of the bottom zone in compression test should apparently stiffen the tissue, while Poisson's ratio of the surface zone was reported as a small value, e.g. about 0.05 [15]. Our experimental observation for

estimating local strain distribution was examined in this complex phenomenon. Therefore, Young's modulus distribution in our report may apparently be a medial value between the results of confined and unconfined compression. While many different values were employed for Poisson's ratio with respective insights, we simply borrowed the value of 0.125 as a reasonable value, which was past used in some FE model [49]. In any case, in considering dynamic transient condition studied in this paper, the spring element representing the collagen network predominantly resists the lateral deformation caused by interstitial fluid pressure in the platen compression test.

Solid phase of the tissue is subjected to the interstitial fluid pressure including the osmotic pressure in addition to the compressive forces as a load-bearing. The collagen network reinforces the solid phase and resists mainly tensile deformation. The cartilaginous tissue involves tension–compression nonlinearity [3–5]. The structural combination of swelling plenty water content and binding the collagen network under the low permeability produces the high pressure of the interstitial fluid, which offers considerable contact load supported by the fluid phase and reduces solid-to-solid frictional force. The mechanical function of the collagen network is a significant factor in considering biphasic lubrication. The collagen network in the tissue has depth-specific anisotropy and inhomogeneity. The FE model in this study included horizontal and vertical spring for representing the collagen network. In the platen compression test, it is thought that the vertical collagen expresses little of its functionality. However, the vertical collagen fibril specially functions in spherical or cylindrical indentation in transient period. The presence of the vertical fibril increased the transient stiffness of the cartilage and the interstitial fluid pressure [40]. Authors confirmed the role of the vertical fibril (not shown in the present paper), in which the vertical fibril resisted vertical bulge that would have been caused by the interstitial fluid pressure around the indenter. Then, the restraint of vertical bulge by vertical fibril enhanced the interstitial fluid pressure. Although we realizes that the morphology of collagen network should have some function as a load-bearing, authors decided to apply homogeneous and isotropic arrangement of the spring elements representing the collagen network in the model, because of the complexity. This point was a limitation of this study. However, the inclusion of the vertical fibril in the model should play a significant role especially in the condition of the sliding cylindrical indenter.

The FEM survey on how much the constitutive properties of the model sustained the proportion of fluid support showed a comprehensible result shown in Fig. 8. Migrating contact area delivers a time period to re-swell the tissue. Pawaskar reported that the proportion of load support by the pore pressure was maintained in the configuration with the metallic cylindrical indenter sliding on cartilage surface in FEM simulation [42]. By experimental friction tests, Caligaris reported that migrating contact area significantly promoted sustainability of the interstitial fluid pressurization mechanism and consequent low friction coefficient [41]. Within the condition A shown in Fig. 8, the sliding condition showed larger proportion of the fluid load support than stationary one. In this study, FEM calculation of the condition A was almost equal to that by Pawaskar's report except for large permeability value, which was set to the initial permeability k_0 having 7.5 times larger value than Pawasker's one. Although the proportion of fluid load support was lower than that of the previous paper, which reported 81% of total contact load, sliding condition exceedingly prevented declination of the proportion of fluid load support. The inclusion of Young's modulus distribution also promoted the proportion of fluid load support in comparing the conditions A with B in Fig. 8. This phenomenon was past suggested in the previous study [46], which included depth-dependent properties on every constitutive parameter. Very low Young's modulus in the top layer may be partly included the effect on biphasic surface amorphous layer [39], which was discussed with an effect on repeated dynamic loading.

Inclusion of the compaction effect on permeability showed an interesting result. In Fig. 8(a), the compaction effect to the fluid support was not seen in comparing the conditions C with B. In Fig. 8(d), the compaction effect did not promote the fluid load support in the sliding condition. However, the compaction effect to the fluid load support clearly arose in the stationary condition shown in Fig. 8(c). Of course, it was obvious that the transition to lower permeability by the compaction effect suppressed the fluid flow and caused higher proportion of the fluid load support, because the condition B remained to the initial permeability value k_0. We had better consider that the compaction effect on permeability did not well promote the interstitial fluid load support especially in the sliding condition. There arises a question why the compaction effect on permeability exists in the properties of the articular cartilage. The lower compressive modulus in surface layer normally promotes the proportion of fluid load support, whereas the constitution of the lower compressive modulus of the solid phase may not be able to maintain lower permeability in the actual tissue. Therefore, the compaction effect on permeability would be a substitutional property to increase the fluid support in the condition of the stationary contact. However, it should be additionally noted that in severe sliding condition with short stroke without sufficient re-hydration, the deformation will become larger and thus the compaction effect on permeability may be effective.

The reinforcement of solid phase by the spring elements representing the collagen network significantly promoted the interstitial fluid load support in sliding condition. The representation of collagen network was discussed in the past, in which sharp reaction force was observed at immediately after compression by the inclusion of tensile reinforcement [24,40]. It is clearly thought that the sliding condition is one of the dynamic conditions. Finally, the condition E shown in Fig. 8 resulted in most superior proportion of the fluid load support in both stationary and sliding condition.

It may be too premature to discuss the interstitial fluid flow, because some of characteristic constitution in the cartilaginous tissue was not completely represented in our model, especially on the depth-dependent inhomogeneity and anisotropy of the collagen network. However, a peculiar fluid flow, typically shown in Fig. 9, was observed in the conditions C and E, which included the compaction effect on permeability. Although it was difficult to interpret the peculiar internal fluid flow at present state, the inclusion of the compaction effect altered the dynamics of fluid flow in surface to middle zone. From the observation of micro-anatomical response of cartilage-bone constitution, a chevron discontinuity under rectangular indentation was reported with an affair of the potential for delamination to occur in the upper region of cartilage [47]. The mechanics in this region should be still a future problem. Inclusion of the spring element representing the collagen network, which was specified by the conditions D and E in Fig. 8, clearly showed the drawing of fluid into cartilage tissue behind the sliding motion near the cylindrical indenter, typically shown in Fig. 10(b). In the cartilage surface far from the indenter, a small drawing of the fluid was observed over a wide range in any sliding condition. The inclusion of the spring reinforcement promoted the drawing of the fluid in near the high fluid pressure just under the indenter.

There are some limitations in this study. Today, more detailed FE models [24–34] were proposed, e.g. inhomogeneity and anisotropy of the collagen network and the permeability, osmotic pressure and its electrical current flow, viscoelasticity of the matrix, nonlinearity of the collagen in tensile direction and so on. The physiological contact geometry and load [35] was not examined. We believe that more detailed model should find another new functionality on the

integration of constitutive material property, while the experimental observation has to be continued to acquire appropriate insights and actual phenomena. In this study, the behavior of tissue matrix under the sliding condition was not observed experimentally. To evaluate the FEM simulation, a new experimental tester to observe internal strain field under sliding indenter will be developed in near future as a series of this study.

The methodology of this study may have an obscure part. The curve fitting was executed by the repetition of visual confirmation shown in Fig. 7. Although authors experienced acceptable orthogonality of the parameters for representing material properties as described in Section 3.2, inclusion of another extra parameter may result in uncertain identification of the material parameters as long as the method in curve fitting will not be advanced. More distinct method should be incorporated in the curve fitting procedure, e.g. the least-square method. It was thought that the time of 92 s for sliding or stationary load was still transient period. In ABAQUS (version 6.8-4), the time integration length is partly controlled by the parameter UTOL. In this study, UTOL of 1000 kPa was set in sliding period in our calculation, while Pawaskar specified UTOL of 600 kPa in their sliding simulation [42]. However, time integration length was controlled around 0.01 s by the version of ABAQUS used in this study, while maximum time integration length was restricted in about 0.05 s. Moreover, the two-dimensional model was used instead of three-dimensional model in order to reduce computational time. The spring elements representing collagen network were spread in vertical and horizontal direction in the model. In this situation, the spring elements did not work in pure parallelogram deformation. Therefore, arguments in this report may partly be closed in a qualitative one in present state. The specimen used in this study was harvested from porcine knee joint of 6–8 months old. Since degree of mature affects biomechanical properties [50,51], we should consider that the experimental data in this study was the data from relatively immature tissue.

5. Conclusion

In this study, the effect of constitutive properties of the cartilaginous tissue as a biphasic material was investigated mainly on how the existence of constitutive material properties affects the proportion of the fluid support in contact area. Time-dependent reaction force was acquired experimentally by cylindrical indentation, which had almost equal geometry to the FEM simulation. The FE model simulation identified material properties by the curve fitting method. In consequent sliding simulation, the reinforcement by spring elements and depth-dependent elastic properties were significantly effective in interstitial fluid pressurization. The compaction effect on the permeability did not show clear improvement on sustainability of the interstitial fluid support in sliding configuration, whereas the compaction effect arose in stationary indentation configuration.

Acknowledgment

Financial support was partly given by the Grant-in-Aid for Scientific Research (A) of Japan Society for the Promotion of Science (21246029) and the Bilateral Joint Research Project with UK supported by Japan Society for the Promotion of Science.

References

[1] Ateshian GA. The role of interstitial fluid pressurization in articular cartilage lubrication. J Biomech 2009;42:1163–76.
[2] Katta J, Jin Z, Ingham E, Fisher J. Biotribology of articular cartilage—a review of the recent advances. Med Eng Phys 2008;30:1349–63.
[3] Huang CY, Soltz MA, Kopacz M, Mow VC, Ateshian GA. Experimental verification of the roles of intrinsic matrix viscoelasticity and tension–compression nonlinearity in the biphasic response of cartilage. J Biomech Eng—Trans ASME 2003;125:84–93.
[4] Chahine NO, Wang CCB, Hung CT, Ateshian GA. Anisotropic strain-dependent material properties of bovine articular cartilage in the transitional range from tension to compression. J Biomech 2004;37:1251–61.
[5] Ateshian GA, Hung CT. The natural synovial joint: properties of cartilage. Proc Inst Mech Eng H: J Eng Med 2006;220:657–70.
[6] Klein J. Molecular mechanisms of synovial joint lubrication. Proc Inst Mech Eng J: J Eng Tribol 2006;220:691–710.
[7] Graindorge S, Ferrandez W, Ingham E, Jin Z, Twigg P, Fisher J. The role of the surface amorphous layer of articular cartilage in joint lubrication. Proc Inst Mech Eng H: J Eng Med 2006;220:597–607.
[8] Murakami T, Higaki H, Sawae Y, Ohtsuki N, Moriyama S, Nakanishi Y. Adaptive multimode lubrication in natural synovial joints and artificial joints. Proc Inst Mech Eng H: J Eng Med 1998;212:23–35.
[9] Murakami T, Nakashima K, Sawae Y, Sakai N, Yarimitsu S, Hosoda N. Roles of adsorbed film and gel layer in hydration lubrication for articular cartilage. Proc Inst Mech Eng H: J Eng Med 2009;223:287–95.
[10] Crockett R, Roos S, Rossbach P, Dora C, Born W, Troxler H. Imaging of the surface of human and bovine articular cartilage with ESEM and AFM. Tribol Lett 2005;19:311–7.
[11] Yarimitsu S, Nakashima K, Sawae Y, Murakami T. Influences of lubricant composition on forming boundary film composed of synovia constituents. Tribol Int 2009;42:1615–23.
[12] Guilak F, Ratcliffe A, Mow VC. Chondrocyte deformation and local tissue strain in articular cartilage: a confocal microscopy study. J Orthop Res 1995;13:410–21.
[13] Schinagl RM, Gurskis D, Chen AD, Sah R. Depth-dependent confined modulus of full-thickness bovine articular cartilage. J Orthop Res 1997;15:499–506.
[14] Chen AC, Bae WC, Schinagl RM, Sah RL. Depth- and strain-dependent mechanical and electromechanical properties of full-thickness bovine articular cartilage in confined compression. J Biomech 2001;34:1–12.
[15] Wang CCB, Deng JM, Ateshian GA, Hung CT. An automated approach for direct measurement of two dimensional strain distributions within articular cartilage under unconfined compression. J Biomech Eng—Trans ASME 2002;124:557–67.
[16] Erne OK, Reid JB, Ehmke LW, Sommers MB, Madey SM, Bottlang M. Depth-dependent strain of patellofemoral articular cartilage in unconfined compression. J Biomech 2005;38:667–72.
[17] Jurvelin JS, Bushmann MD, Hunziker EB. Mechanical anisotropy of the human knee articular cartilage in compression. Proc Inst Mech Eng H: J Eng Med 2003;217:215–9.
[18] Wang CCB, Chahine NO, Hung CT, Ateshian GA. Optical determination of anisotropic material properties of bovine articular catrilage in compression. J Biomech 2003;36:339–53.
[19] Mow VC, Kuei SC, Lai WM, Armstrong CG. Biphasic creep and stress relaxation of articular cartilage in compression: theory and experiments. J Biomech Eng—Trans ASME 1980;102:73–84.
[20] Park S, Krishnan R, Nicoll SB, Ateshian GA. Cartilage interstitial fluid load support in unconfined compression. J Biomech 2003;36:1785–96.
[21] Ateshian GA. A theoretical formulation for boundary friction in articular cartilage. J Biomech Eng—Trans ASME 1997;119:81–6.
[22] Ateshian GA, Wang H, Lai WM. The role of interstitial fluid pressurization and surface porosities on the boundary friction of articular cartilage. J Tribol—Trans ASME 1998;120:241–8.
[23] Krishnan R, Kopacz M, Ateshian GA. Experimental verification of the role of interstitial fluid pressurization in cartilage lubrication. J Orthop Res 2004; 22:565–70.
[24] Li LP, Soulhat J, Buschmann MD, Shirazi-Adl A. Nonlinear analysis of cartilage in unconfined ramp compression using a fibril reinforced poroelastic model. Clin Biomech 1999;14:673–82.
[25] Li LP, Soulhat J, Buschmann MD, Shirazi-Adl A. A fibril reinforced nonhomogeneous poroelastic model for articular cartilage: inhomogeneous response in unconfined compression. J Biomech 2000;33:1533–41.
[26] Soltz MA, Ateshian GA. A conewise linear elasticity mixture model for the analysis of tension–compression nonlinearity in articular cartilage. J Biomech Eng—Trans ASME 2000;122:576–86.
[27] Huang CY, Mow VC, Ateshian GA. The role of flow-independent viscoelasticity in the biphasic tensile and compressive responses of articular cartilage. J Biomech Eng—Trans ASME 2001;123:410–7.
[28] Wang CCB, Hung CT, Mow VC. An analysis of the effects of depth-dependent aggregate modulus on articular cartilage stress-relaxation behavior in compression. J Biomech 2001;34:75–84.
[29] Wilson W, van Donkelaar CC, van Rietbergen B, Ito K, Huiskes R. Stress in the local collagen network of articular cartilage: a poroviscoelastic fibril-reinforced finite element study. J Biomech 2004;37:357–66.
[30] Wilson W, van Donkelaar CC, van Rietbergen B, Huiskes R. A fibril-reinforced poroviscoelastic swelling model for articular cartilage. J Biomech 2005;38: 1195–204.
[31] Federico S, Grillo A, Rosa GL, Giaquinta G, Herzog W. A transversely isotropic, transversely homogeneous microstructual-statistical model of articular cartilage. J Biomech 2005;38:2008–18.

[32] Wilson W, van Donkelaar CC, Huyghe JM. A comparison between mechano-electrochemical and biphasic swelling theories for soft hydrated tissues. J Biomech Eng—Trans ASME 2005;127:158–65.
[33] Ateshian GA, Chahine NO, Basalo IM, Hung CT. The correspondence between biphasic and triphasic material properties in mixture models of articular cartilage. J Biomech 2004;37:391–400.
[34] Sun DD, Guo XE, Likhitpanichkul M, Lai WM, Mow VC. The influence of the fixed negative charges on mechanical and electrical behaviors of articular cartilage under unconfined compression. J Biomech Eng—ASME 2004; 126:7–16.
[35] Warner MD, Taylor WR, Clift SE. Finite element biphasic indentation of cartilage: a comparison of experimental indenter and physiological contact geometry. Proc Inst Mech Eng H: J Eng Med 2001;215:487–96.
[36] Shirazi R, Shirazi-Adl A, Hurtig M. Role of cartilage collagen fibrils networks in knee joint biomechanics under compression. J Biomech 2008;41:3340–8.
[37] Park S, Hung CT, Ateshian GA. Mechanical response of bovine articular cartilage under dynamic unconfined compression loading at physiological stress level. Osteoarthritis Cartilage 2004;12:65–73.
[38] Krishnan R, Mariner EN, Ateshian GA. Effect of dynamic loading on the frictional response of bovine articular cartilage. J Biomech 2005;38:1665–73.
[39] Graindorge S, Ferrandez W, Jin ZM, Ingham E, Fisher J. The natural synovial joint: a finite element investigation of biphasic surface amorphous layer lubrication under dynamic loading condition. Proc Inst Mech Eng J: J Eng Tribol 2006;220:671–81.
[40] Shirazi R, Shirazi-Adl A. Deep vertical collagen fibrils play a significant role in mechanics of articular cartilage. J Orthop Res 2008;26:608–15.
[41] Caligaris M, Ateshian GA. Effect of sustained internal fluid pressurization under migrating contact area, and boundary lubrication by synovial fluid, on cartilage friction. Osteoarthritis Cartilage 2008;16:1220–7.
[42] Pawaskar SS, Jin ZM, Fisher J. Modelling of fluid support inside articular cartilage during sliding. Proc Inst Mech Eng J: J Eng Tribol 2007;221:165–74.
[43] Willett TL, Whiteside R, Wild PM, Wyss UP, Anastassiades T. Artefacts in the mechanical characterization of pocine articular cartilage due to freezing. Proc Inst Mech Eng H: J Eng Med 2005;219:23–9.
[44] Hosoda N, Sakai N, Sawae Y, Murakami T. Depth-dependence and time-dependence in mechanical behavior of articular cartilage in unconfined compression test under constant total deformation. J Biomech Sci Eng 2008; 3:209–20.
[45] Wu JZ, Herzog W, Epstein M. Evaluation of the finite element software ABAQUS for biomechanical modelling of biphasic tissues, technical note. J Biomech 1998;31:165–9.
[46] Pawaskar SS, Jin ZM, Fisher J. Robust and general method for determining surface fluid flow boundary conditions in articular cartilage contact mechanics modeling. J Biomech Eng—Trans ASME 2010;132:3.
[47] Krishnan R, Park S, Eckstein F, Ateshian GA. Inhomogeneous cartilage properties enhance superficial interstitial fluid support and frictional properties, but do not provide a homogeneous state of stress. J Biomech Eng—Trans ASME 2003;125:569–77.
[48] Thambyah A, Broom N. Micro-anatomical response of cartilage-on-bone to compression: mechanisms of deformation within and beyond the directly loaded matrix. J Anat 2006;209:611–22.
[49] Guilak F, Mow VC. The mechanical environment of the chondrocyte: a biphasic finite element model of cell–matrix interactions in articular cartilage. J Biomech 2000;33:1663–73.
[50] Williamson AK, Chen AC, Masuda K, Thonar EJMA, Sah RL. Tensile mechanical properties of bovine articular cartilage: variations with growth and relationships to collagen network components. J Orthop Res 2003;21: 872–80.
[51] Klein TJ, Caudhry M, Bae WC, Sah RL. Depth-dependent biomechanical and biochemical properties of fetal, newborn, and tissue-engineered articular cartilage. J Biomech 2007;40:182–90.

Biomaterials 33 (2012) 4451–4459

Contents lists available at SciVerse ScienceDirect

Biomaterials

journal homepage: www.elsevier.com/locate/biomaterials

Biomimetic hydration lubrication with various polyelectrolyte layers on cross-linked polyethylene orthopedic bearing materials

Masayuki Kyomoto [a,b,d], Toru Moro [b,c], Kenichi Saiga [a,b,d], Masami Hashimoto [e], Hideya Ito [c], Hiroshi Kawaguchi [c], Yoshio Takatori [b,c], Kazuhiko Ishihara [a,*]

[a] Department of Materials Engineering, School of Engineering, The University of Tokyo, 7-3-1 Hongo, Bunkyo-ku, Tokyo 113-8656, Japan
[b] Division of Science for Joint Reconstruction, Graduate School of Medicine, The University of Tokyo, 7-3-1 Hongo, Bunkyo-ku, Tokyo 113-8656, Japan
[c] Sensory & Motor System Medicine, Faculty of Medicine, The University of Tokyo, 7-3-1 Hongo, Bunkyo-ku, Tokyo 113-8656, Japan
[d] Research Department, Japan Medical Materials Corporation, 3-3-31 Miyahara, Yodogawa-ku, Osaka 532-0003, Japan
[e] Materials Research and Development Laboratory, Japan Fine Ceramics Center, 2-4-1 Mutsuno, Atsuta-ku, Nagoya 456-8587, Japan

ARTICLE INFO

Article history:
Received 28 December 2011
Accepted 7 March 2012
Available online 30 March 2012

Keywords:
Joint replacement
Polyethylene
Surface modification
Biomimetic material
Wear mechanism

ABSTRACT

Natural joints rely on fluid thin-film lubrication by the hydrated polyelectrolyte layer of cartilage. However, current artificial joints with polyethylene (PE) surfaces have considerably less efficient lubrication and thus much greater wear, leading to osteolysis and aseptic loosening. This is considered a common factor limiting prosthetic longevity in total hip arthroplasty (THA). However, such wear could be mitigated by surface modification to mimic the role of cartilage. Here we report the development of nanometer-scale hydrophilic layers with varying charge (nonionic, cationic, anionic, or zwitterionic) on cross-linked PE (CLPE) surfaces, which could fully mimic the hydrophilicity and lubricity of the natural joint surface. We present evidence to support two lubrication mechanisms: the primary mechanism is due to the high level of hydration in the grafted layer, where water molecules act as very efficient lubricants; and the secondary mechanism is repulsion of protein molecules and positively charged inorganic ions by the grafted polyelectrolyte layer. Thus, such nanometer-scaled hydrophilic polymers or polyelectrolyte layers on the CLPE surface of acetabular cup bearings could confer high durability to THA prosthetics.

1. Introduction

The number of artificial hip and knee joints used for primary and revised hip replacement is increasing substantially every year all over the world [1]. Most patients who receive an artificial joint experience dramatic pain relief and rapid improvement in their daily activities as well as quality of life. The most popular artificial hip joint system is a bearing couple composed of polyethylene (PE; currently cross-linked PE or CLPE) and a cobalt–chromium–molybdenum (Co–Cr–Mo) alloy. However, osteolysis has emerged as a serious issue that limits the duration and clinical outcome of artificial hip joints [2,3]. Osteolysis is triggered by a host of inflammatory responses to PE wear particles originating from the interface [4], which undergo phagocytosis by macrophages and thus induce secretion of bone resorptive cytokines [5]. Hence, different combinations of bearing surfaces and improvements in bearing materials have been studied with the aim of reducing the number of PE wear particles and extending the longevity of artificial hip joint [6–13]. However, few studies have explored methods to enhance the lubrication at the articular interface of artificial hip joints.

The bearing surfaces of a natural synovial joint are covered with a specialized type of hyaline cartilage, i.e., articular cartilage, which protects the joint interface from mechanical wear and facilitates a smooth motion of joints during daily activity [14,15]. The articular cartilage consists of chondrocytes, surrounding matrix macromolecules (e.g., proteoglycans, glycosaminoglycans, and collagens) and surface active phospholipids (SAPL; e.g., phosphatidylcholine derivatives). Due to their charge, they can trap water to maintain the water-fluid and electrolyte balance in the articular cartilages, which provides hydrophilicity and works as an effective boundary lubricant [16,17]. The fluid thin-film lubrication by the hydrated polyelectrolyte layer of articular cartilage is essential for the smooth motion of natural synovial joints. Given that learning from and mimicking nature is a widely successful theme in science and technology, it seems promising to

* Corresponding author. Tel.: +81 3 5841 7124; fax: +81 3 5841 8647.
E-mail address: ishihara@mpc.t.u-tokyo.ac.jp (K. Ishihara).

0142-9612/$ – see front matter © 2012 Elsevier Ltd. All rights reserved.
doi:10.1016/j.biomaterials.2012.03.028

investigate surface modification of bearing surfaces in artificial joints to mimic the role of cartilage.

Grafting of polymeric molecules onto a substrate through covalent bonding is a well-known method for modifying a polymer surface [18]. Grafting polymerization is mostly performed using either of the following methods: (1) surface-initiated graft polymerization, termed the "grafting from" method, in which monomers are polymerized from initiators or comonomers; and (2) adsorption of the polymer to the substrate, termed the "grafting to" method (i.e., dipping, cross-linking, and ready-made polymers reacting with the substrate) [19,20]. The former method has an advantage over the latter method in that it synthesizes a semi-dilute or high-density polymer brush [21].

In this study, we synthesized nanometer-scale hydrophilic layers on the CLPE surface of an artificial hip joint to reduce wear and avoid bone resorption. Our strategy is to modify the bearing surfaces of artificial joints with a hydrophilic polyelectrolyte layer to increase lubrication to levels that match articular cartilage under physiological conditions. Such nanometer-scale surface modification was accomplished using a photoinduced radical polymerization technique similar to the "grafting from" method; this approach renders only the surface of the CLPE substrate susceptible to modification and does not affect the bulk properties [22,23]. In addition, we investigated the effect of polyelectrolyte layers with various lubrication conditions on hydration lubrication [24] to realize the hydrophilicity and lubricity of the physiological joint surface. Such investigations are of great importance in the design of lubricated surfaces for artificial joints, and in better understanding the lubrication mechanisms of both natural and artificial joints. Here, we asked whether (1) the hydrophilic polymer or polyelectrolyte characteristics (i.e., nonionic, cationic, anionic, or zwitterionic) would affect the hydration- and friction-kinetics of the hydration layer and (2) the hydration lubrication characteristics of the polyelectrolyte layers might assure the durability of artificial hips.

2. Materials and methods

2.1. Chemicals

Benzophenone and acetone were purchased from Wako Pure Chemical Industries, Ltd. (Osaka, Japan). Oligo(ethylene glycol) methacrylate (M_n = 360; OEGMA) and 2-(dimethylamino)ethyl methacrylate (DMAEMA) were purchased from Sigma–Aldrich Corp. (Saint Louis, MO, USA) and Tokyo Chemical Industry Co., Ltd. (Tokyo, Japan), respectively (Fig. 1A). 2-Methacryloyloxyethyl phosphate (MPA) was extracted from an aqueous suspension of Phosmer M solution (Unichemical Co., Ltd., Ikoma, Japan) with *n*-hexane (Kanto Chemical Co., Inc., Tokyo, Japan). 2-Methacryloyloxyethyl phosphorylcholine (MPC) was industrially synthesized by using the method reported by Ishihara et al. and supplied by NOF Corp. (Tokyo, Japan) [25].

2.2. Graft polymerization with various polyelectrolytes

A compression-molded PE (GUR1020 resin; Quadrant PHS Deutschland GmbH, Vreden, Germany) sheet stock was irradiated with a 50-kGy dose of gamma-rays in N_2 gas and annealed at 120 °C for 7.5 h in N_2 gas in order to facilitate cross-linking. CLPE specimens were then machined from this sheet stock after cooling.

These CLPE specimens were immersed in an acetone solution containing 10 mg/mL benzophenone for 30 s and then dried at room temperature in order to remove the acetone. Each monomer was dissolved in degassed pure water to obtain a 0.50-mol/L monomer aqueous solution, and the CLPE specimens coated with benzophenone were immersed in this solution. Photoinduced graft polymerization on the CLPE surface was performed using UV irradiation (UVL-400HA ultra-high pressure mercury lamp; Riko-Kagaku Sangyo Co., Ltd., Funabashi, Japan) with an intensity of 5 mW/cm^2 at 20 °C (DMAEMA) [26] or 60 °C (OEGMA, MPA, MPC) for 23–180 min (Fig. 1B); a filter (Model D-35; Toshiba Corp., Tokyo, Japan) was used to restrict the UV light to wavelengths of 350 ± 50 nm [27,28]. After polymerization, each of the poly(OEGMA) (POEGMA)-, poly(DMAEMA) (PDMAEMA)-, poly(MPA) (PMPA)-, and poly(MPC) (PMPC)-grafted CLPE specimens was removed, washed with pure water and ethanol, and dried at room temperature. These and untreated CLPE (as control) specimens were sterilized by with a 25-kGy dose of gamma-rays under N_2 gas [29].

2.3. Cross-sectional observation by transmission electron microscopy

A cross-section of the various polyelectrolyte-grafted layers on the CLPE surface with a 90-min photoirradiation time was observed under a transmission electron microscope (TEM). The specimens were embedded in epoxy resin, stained with ruthenium oxide vapor at room temperature, and finally sliced into ultra-thin films (approximately 100-nm-thick) by using a Leica Ultra Cut UC microtome (Leica Microsystems, Ltd., Wetzlar, Germany). The specimens of the various polyelectrolyte-grafted CLPE were pre-coated with a platinum–palladium thin film before embedding in epoxy resin to preserve the graft layer. A JEM-1010 electron microscope (JEOL, Ltd., Tokyo, Japan) was used for the TEM observations at an acceleration voltage of 100 kV.

2.4. Surface analysis of various polyelectrolyte-grafted CLPEs

The functional group vibrations of the various polyelectrolyte-grafted CLPE surfaces with a 90-min photoirradiation time were examined by Fourier-transform infrared (FT-IR) spectroscopy with attenuated total reflection (ATR) equipment. The FT-IR/ATR spectra were obtained using an FT-IR analyzer (FT/IR615; JASCO Co. Ltd., Tokyo, Japan) for 32 scans over the range 800–2000 cm^{-1} at a resolution of 4.0 cm^{-1}.

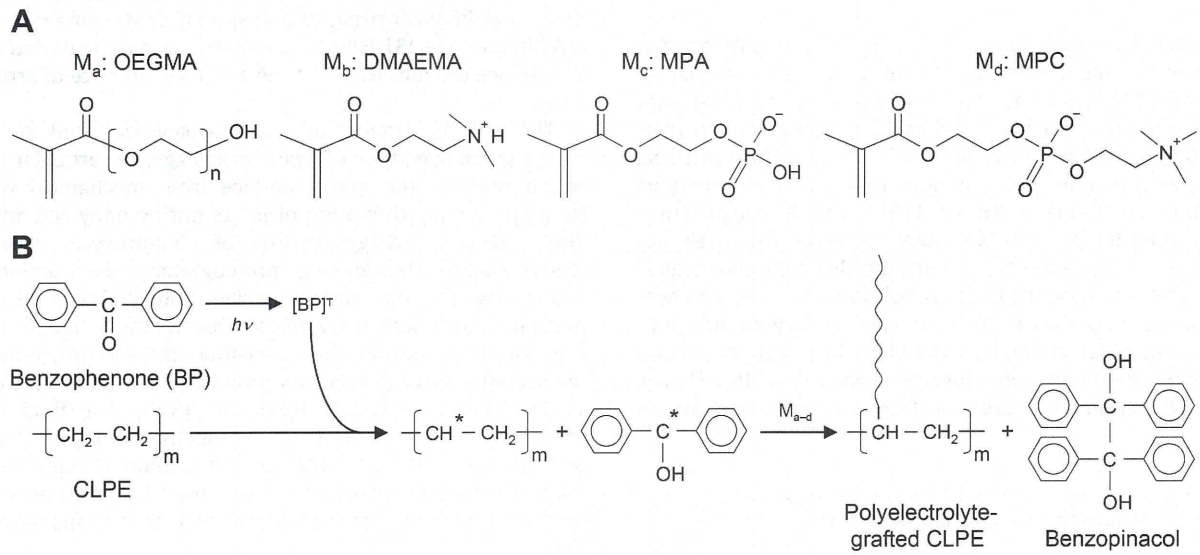

Fig. 1. Schematic illustration showing the preparation of various polyelectrolyte-grafted CLPE. (A) Monomers and (B) photoinduced graft polymerization.